

Article

Generation and Mitigation Mechanism Studies of Nonlinear Thermoacoustic Instability in a Modelled Swirling Combustor with a Heat Exchanger [†]

Yuze Sun ¹, Dan Zhao ^{1,*}  and Xiaowei Zhu ²

¹ Department of Mechanical Engineering, College of Engineering, University of Canterbury, Christchurch 8041, New Zealand; yuze.sun@pg.canterbury.ac.nz

² Department of Mechanical Engineering, Eindhoven University of Technology, 5600 MB Eindhoven, The Netherlands; x.zhu2@tue.nl

* Correspondence: dan.zhao@canterbury.ac.nz

[†] This paper is a modified version of our paper “Numerical Study of Nonlinear Self-sustained Thermoacoustic Instability in a Swirling Combustor” published at the AIAA Propulsion and Energy 2020 Forum, 24–28 August 2020, VIRTUAL EVENT.

Abstract: In the present work, 3D Unsteady Reynolds-Averaged Navier-Stokes (URANS) simulations are performed to investigate the generation and mitigation mechanism of combustion-sustained thermoacoustic instabilities in a modelled swirl combustor. The effects of (1) swirling number S_N , (2) inlet air flow rate V_a and (3) inlet temperature T_i on the amplitudes and frequencies of swirling combustion-excited limit cycle oscillations are examined. It is found that the amplitude of acoustic fluctuations is increased with increasing S_N and V_a and decreased with the increase of T_i . The dominant frequency of oscillations is also found to increase with the increase of S_N and V_a . However, increasing T_i leads to the dominant frequency being decreased first and then increased. An alternative passive control method of installing an adjustable temperature heat exchanger on the combustion chamber wall is then proposed. Numerical results show that thermoacoustic oscillations could be excited and mitigated by setting the heat exchanger temperature to T_H . Global and local Rayleigh indexes are applied to further reveal the excitation and attenuation effects on mechanisms. The present study is conducive to developing a simulation platform for thermoacoustic instabilities in swirling combustors. It also provides an alternative method to amplify or mitigate thermoacoustic oscillations.

Keywords: propulsion; thermoacoustic; combustion instability; passive control; aeroacoustics



Citation: Sun, Y.; Zhao, D.; Zhu, X. Generation and Mitigation Mechanism Studies of Nonlinear Thermoacoustic Instability in a Modelled Swirling Combustor with a Heat Exchanger. *Aerospace* **2021**, *8*, 60. <https://doi.org/10.3390/aerospace8030060>

Academic Editor: Antonio Ficarella

Received: 26 December 2020

Accepted: 21 February 2021

Published: 26 February 2021

Publisher's Note: MDPI stays neutral with regard to jurisdictional claims in published maps and institutional affiliations.



Copyright: © 2021 by the authors. Licensee MDPI, Basel, Switzerland. This article is an open access article distributed under the terms and conditions of the Creative Commons Attribution (CC BY) license (<https://creativecommons.org/licenses/by/4.0/>).

1. Introduction

Energy efficiency and pollutant emissions have become increasingly global concerns [1]. Lean premixed combustion is an effective method for reducing chemical emission of NO_x and enhancing combustion efficiency [2]. However, lean premixed flames usually encounter unwanted issues such as thermoacoustic instability, flashback, and blow-off [3,4]. An attendant problem of thermoacoustic instability is often large amplitude pressure oscillation [5]. Thermoacoustic instability originates from the feedback loop between flow perturbations, heat release and acoustic oscillations [6]. It occurs when the ‘driving’ effect generated by in-phase coupling between the unsteady heat release rate and acoustic fluctuations is greater than the ‘damping’ effect from viscosity, heat transfer, sound radiation, etc. [7]. Thermoacoustic instability would severely aggravate the pollution and noise emission of combustor [8]. It also causes other problem such as structural vibration and overheating [9]. Consequently, these undesirable issues induced by thermoacoustic instability may result in system failure. [10].

Swirling flows have favorable effects on the combustion process [11]. Swirling flow can reduce the flame length by enhancing the mixing between fuel and air [12]. The formation of a recirculation zone in strongly swirling regions can improve the stability of the

flame [13]. Therefore, swirling flow generators are widely introduced in various types of gas-turbine engines to stabilize high-intensity flames so they remain efficient and clean [14]. Intensive experimental studies have been conducted to investigate the interaction between swirling flow and flames to better understand, predict and control thermoacoustic instability. Kim et al. [15] performed an experimental study to evaluate the effect of thermal power operating conditions and combustor length on the amplitude and frequency of pressure. Han et al. [16] developed a novel double-swirled combustion system to investigate the correlation between flame macrostructures and thermoacoustic combustion instabilities. Karlis et al. [17] investigated the dynamic and structure of hydrogen-enriched methane swirling flames. It was found that flame shape and thermoacoustic oscillation dynamics varied dramatically with H₂ molar content. Thermoacoustic behaviors both under stationary conditions and during transient conditions are examined by Bonciolini et al. [18]. Results show that instabilities during transient conditions are caused by increasing wall temperature when operating parameters are changed.

In addition, the relationship between swirl flow and thermoacoustic instability has been studied numerically by means of computational fluid dynamics (CFD) simulations [19]. Huang et al. [20] examined swirling intensity effects on the pressure and heat release fluctuations of swirling flames by conducting a large eddy simulation (LES). The recirculation regions generated by swirling flow were found to play a significant role in flow–flame interactions. Choi et al. [21] conducted direct numerical simulations (DNS) on a premixed swirling combustor. Results indicate that the near-stagnant breakdown zone originates from swirling flow instability, which is affected by swirling number, tube length, end conditions, and flow exothermicity. Choi et al. [22] conducted a numerical simulation using Reynolds-Averaged Navier-Stokes (RANS) technique to study the flame structure and NO_x and CO emission in a partially premixed dual swirl combustor. The effects of various swirl combinations and syngas compositions were examined.

Thermoacoustic instabilities can be mitigated by breaking the feedback loop between unsteady heat release rate and acoustic oscillations [23]. There are two classical methods for its suppression, which are the active and passive control methods [24]. Active control is typically applied by using a dynamic actuator [25]. Paschereit et al. [26] applied the active control method by using an acoustic actuation on a premixed swirl-stabilized combustor. Pressure oscillations and NO_x emissions are reduced after the implementation of control actions. However, active control methods are always involved in complex control systems [27]. Suitable parameters for control have to be determined in advance of the experiment [28]. Passive control methods are typically implemented by carrying out modification of the combustors such as applying quarter-wave resonators, Helmholtz resonators, and perforated liners [29]. Williams et al. [30] installed a ring porous insert at the inlet plane of a swirling combustor. Experiment results showed that the porous insert could attenuate thermoacoustic instability by changing flow field characteristics in such combustors. However, it is costly and inflexible to modify the combustion chamber structure [31]. To address the drawbacks of passive and active methods, alternative methods have recently been proposed. Wu et al. [32,33] performed experiments on three types of Rijke-type combustors, including a conventional Rijke tube, a Y-shaped tube and a T-shaped tube. It was found that limit-cycle oscillations could be mitigated by inserting an electrical heater in certain areas of the combustor. Mahesh et al. [34] reported a novel strategy for controlling thermoacoustic instability by rotating a swirler in a laboratory premixed combustor. To the best knowledge of the authors, there is a lack of detailed investigation on developing an alternative approach (such as a heat exchanger) to attenuate thermoacoustic instability in a modelled swirling combustor. This motivated the present work.

In this work, 3D Unsteady Reynolds-Averaged Navier-Stokes (URANS) numerical simulations are conducted to investigate the self-sustained thermoacoustic instability in a modelled swirling combustor. The paper structure is organized as follows. Section 2 introduces the physical model and numerical methods. Section 3 presents the results and discussions of the numerical validations and effect of swirling number S_N , incoming air

flow rate V_a and inlet temperature T_i , respectively. Further investigation into the temperature of the heat exchanger, T_H , is presented in Section 4. Finally, the main conclusions of this paper are presented in Section 5.

2. 3 D Model and Numerical Method

2.1. Combustor Geometry and Boundary Conditions

Figure 1 shows a diagram of the present computational domain [35]. To save computational time, we neglect the swirler vanes, and only a 1/8th segment of the combustor with rotational periodic boundary conditions is adopted for computations, which has been applied and verified in a previous study [36]. Moreover, an individual simulation by using a whole domain and a 1/8 sector domain are applied to figure out the discrepancy of simulation results. The comparison results are supplemented in Appendix A. The key geometrical parameters are shown in Figure 1a. The inlet boundary condition is a Dirichlet for velocity and temperature, which can be regarded as an acoustic closed boundary. Premixed CH_4/air with an air flow rate of 130–250 L/min, equivalence ratio of 0.9, inlet temperature of 300–600 K and swirling number of 0.34–0.6 flows into the combustor from the annular inlet. Pressure is outlet of 0 Pa relative pressure treated as an acoustically opened boundary condition is applied at the domain exit. The combustor wall boundaries are defined as adiabatic non-slip walls. The wall where the heat exchanger is located is treated as an iso-thermal boundary condition.

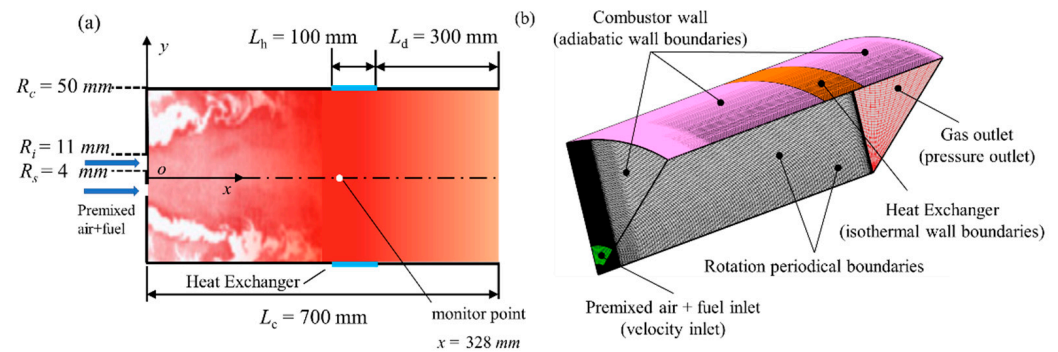


Figure 1. (a) Diagram of computational domain and key geometry parameters, and (b) mesh generation of the 1/8th sector combustor.

2.2. Governing Equations and Numerical Set-Up

Fully compressible Unsteady Reynolds-Averaged Navier-Stokes (URANS) are solved including mass, momentum, energy, and species transport equations:

(1) Mass conservation equation:

$$\frac{\partial \rho}{\partial t} + \nabla \cdot (\rho \vec{v}) = 0 \quad (1)$$

(2) Momentum equation:

$$\frac{\partial}{\partial t} (\rho \vec{v}) + \nabla \cdot (\rho \vec{v} \vec{v}) = -\nabla \rho + \nabla \cdot (\bar{\tau} - \tau'_{ij}) \quad (2)$$

(3) Energy conservation equation:

$$\frac{\partial}{\partial t} (\rho E) + \nabla \cdot (\vec{v} (\rho E + p)) = \nabla \cdot \left(k_{eff} \nabla T - \sum_j h_i \vec{j}_i + (\tau_{eff} \cdot \vec{v}) \right) + S_h \quad (3)$$

(4) Species conservation equation:

$$\frac{\partial}{\partial t}(\rho Y_i) + \nabla \cdot (\rho \vec{v} Y_i) = -\nabla \cdot \vec{J}_i + \omega_i \quad (4)$$

(5) Thermodynamic equation:

$$\rho = \frac{p}{(R_g/M_w)T} \quad (5)$$

where ρ , p and t are density, pressure and time, respectively. \vec{v} is the velocity vector. τ'_{ij} is Reynolds stress tensor. E is the total energy, k_{eff} is the effective conductivity, h_i and J_i are the enthalpy and diffusion flux of species i , S_h is the fluid enthalpy source, Y_i is the mass fraction, ω_i is the reaction rate of species i , R_g is the universal gas constant, and M_w is the mean molecular weight.

The Re-Normalization Group (RNG) k - ϵ model is selected as the turbulence model and The Eddy-dissipation-concept (EDC) model was used for dealing with the combustion process in cases involving a 2-step global reaction mechanism [37]. The boundary conditions, numerical settings and schemes are summarized in Table 1. In the present work, all numerical simulations were performed based, a commercial CFD software, ANSYS FLUENT 19.1.

Table 1. Numerical schemes and boundary conditions.

I. Boundary Conditions		
1. Inlet	2. Outlet	3. Solid Boundaries
Velocity inlet, corresponding air flow rate: $V_a = 130, 180, 250$ L/min Inlet temperature: $T_i = 300, 450, 600$ K Equivalence ratio $\Phi = 0.9$.	Pressure outlet Constant relative pressure, 0 Pa	Combustor wall: adiabatic Heat exchanger: $T_H = T_{\text{ad}}, 300$ K, 1800 K
II. Numerical Schemes		
1. Turbulence Model	2. Combustion Model	3. Pressure-Velocity Coupling
RNG k - ϵ	EDC model	COUPLE
4. Discretization Schemes	5. Time Step	6. reaction Mechanism
Second order implicit for temporal discretization Second-order upwind for turbulence dissipation Third-order MUSCL for others	1×10^{-4} s	2-steps global mechanism

3. Results and Discussion

3.1. Model Validation and Mesh-Independence Study

To reach a better prediction of the combustion and its gradients, the grid of flame area is refined. Three different meshes are used to perform a mesh-independence study. The cell numbers are 0.1 M, 0.5 M and 1.0 M, respectively. The mesh-independence study results in Figure 2 show that the grid with 0.5 M cells presents sufficient resolution for further investigations. In addition, as shown in Figure 3, reacting flow validation is performed by comparing mean velocity profiles at different cross sections obtained from the experimental measurement conducted by Zhang et al. [38] and present simulation. The difference between the simulation results and experiment measurement is minor, which is acceptable for RANS simulations.

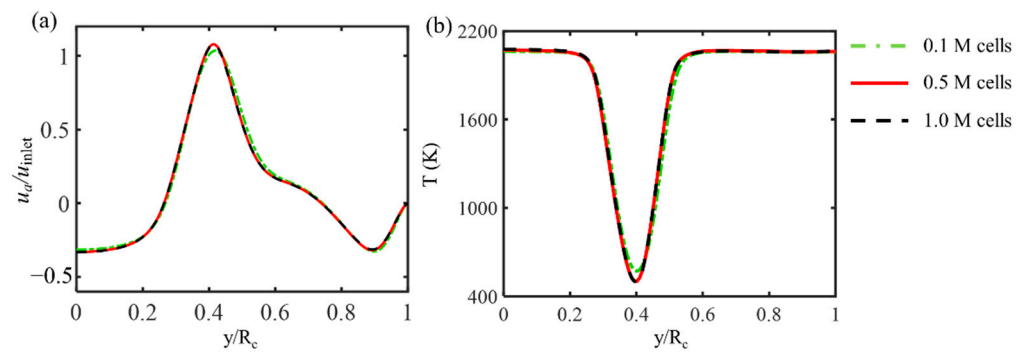


Figure 2. Mesh sensitivity analyses: (a) normalized axial velocity profiles and (b) temperature profiles at $x/R_c = 0.5$.

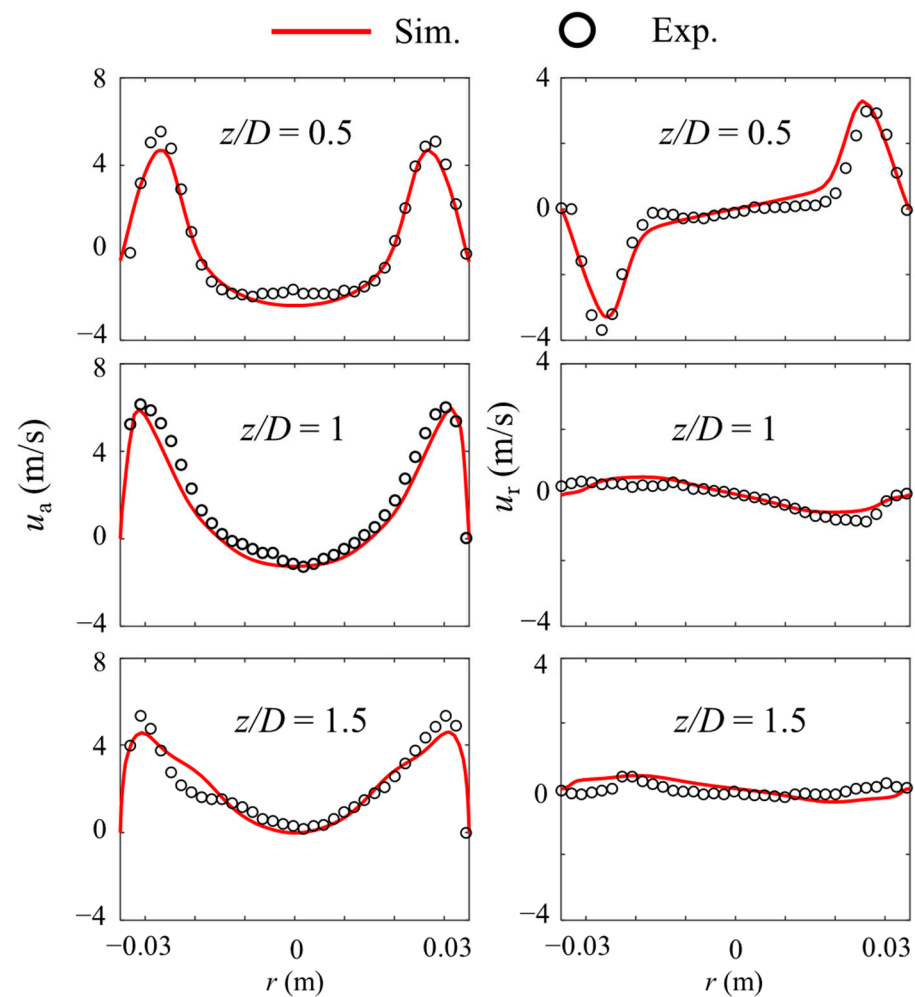


Figure 3. Radial distribution of mean axial (left) and radial (right) velocity components at different cross sections of the combustor. $z/D = 0.5$, $z/D = 1$ and $z/D = 1.5$.

3.2. Effect of Swirling Number S_N

The swirling number effect is examined firstly in this section. Simulations are conducted with three different swirling numbers. It can be seen from Figure 4a that V-shaped swirling flames are observed in all swirling number conditions. In Figure 4a, the white line represents the zero-axial velocity iso-line, which can be used to identify the recirculation zones. As the swirling number is increased, vortex centers in both the corner recirculation zone (CRZ) and central toroidal recirculation zone (CTRZ) move upstream. The lengths of both CRZ and CTRZ are shortened. Flame tips move toward the combustor wall, and the

flame angle is increased. Figure 4b illustrates axial velocity distributions and streamlines. It can be seen that, at high swirl numbers, the negative axial velocity is higher in the recirculation zone. The wake recirculation zone (WRZ) is observed behind the center rod at $S_N = 0.34$; however, disappears at a higher swirling number. This phenomenon can be explained by the fact that the ratio of axial momentum to tangential momentum is larger near the center rod in low swirling number conditions.

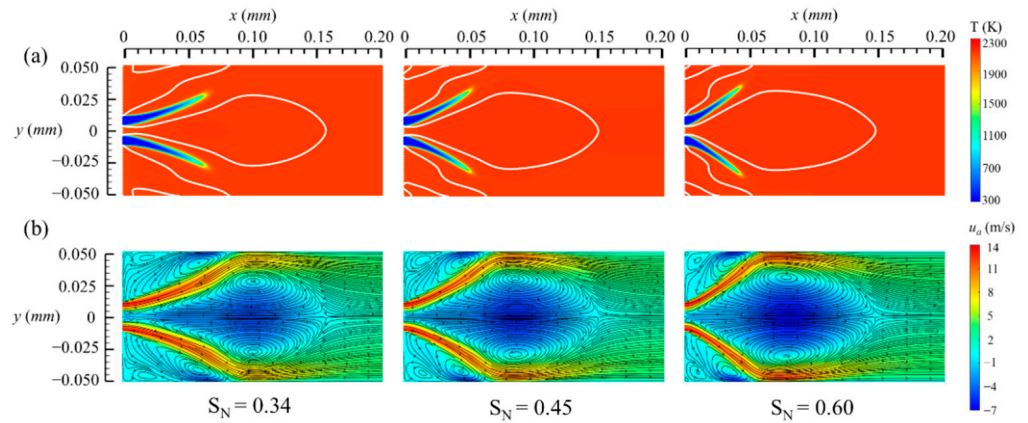


Figure 4. (a) Temperature contour with zero axial velocity isolines, and (b) axial velocity contour along with streamlines of different S_N , where $V_a = 180$, L/min and $T_i = 300$ K.

Figure 5a–c shows the pulsating characteristics of the combustor in three S_N conditions. Pressure fluctuations data are collected from a probe located inside the combustor (at $x = 328$ mm, $y = 0$ mm and $z = 0$ mm). Limited cycle oscillations are successfully built in all three S_N conditions. As S_N is increased, the amplitude of pressure fluctuations is increased and reaches around 710 Pa at $S_N = 0.6$. In Figure 6, the dominant frequency of pressure oscillation is observed to shift to a higher frequency with the increase of S_N , from 290 Hz at $S_N = 0.34$ to 307 Hz at $S_N = 0.6$.

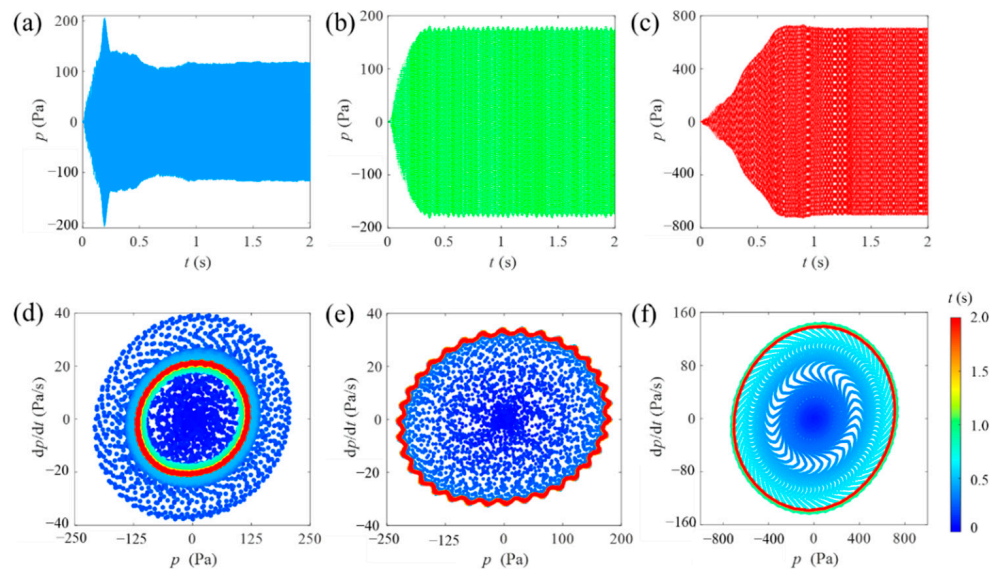


Figure 5. Acoustic pressure fluctuations. (a–c) Time evolution of pressure fluctuations, (d–f) corresponding phase diagram of pressure fluctuations at $V_a = 180$ L/min $T_i = 300$ K. (a) and (d) $S_N = 0.34$, (b) and (e) $S_N = 0.45$, (c) and (f) $S_N = 0.60$.

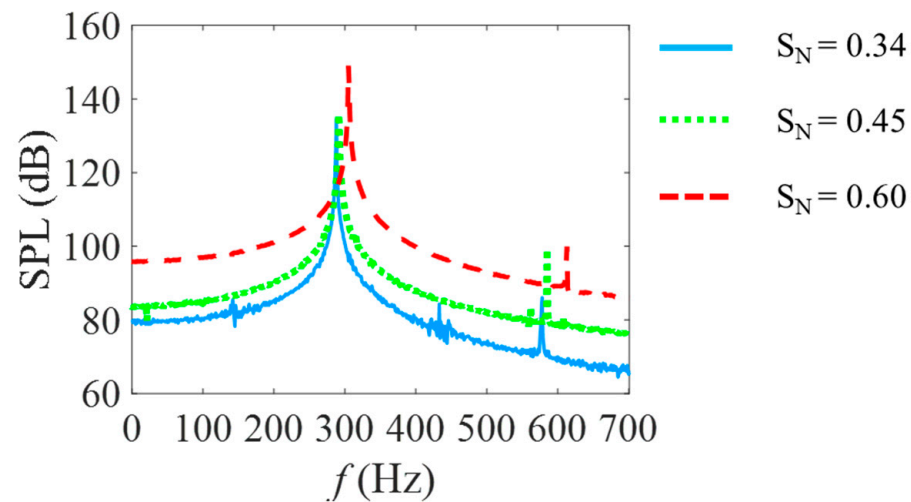


Figure 6. Frequency spectrum of acoustic pressure fluctuations of different S_N at $V_a = 180$ L/min and $T_i = 300$ K.

3.3. Effect of Incoming Air Flow Rate V_a

Figure 7 shows the axial velocity and temperature distributions at $t = 0$ s with an air flow rate of 130, 180 and 250 L/min, respectively. It can be seen from Figure 7a that the CTRZ and CRZ move downstream slightly with the increase in the air flow rate. The flame length also increases. Figure 7b illustrates that the reattached point also moves downstream, and the negative axial velocity in the recirculation zone and the positive axial velocity of the jet are larger under the condition of high flow rate.

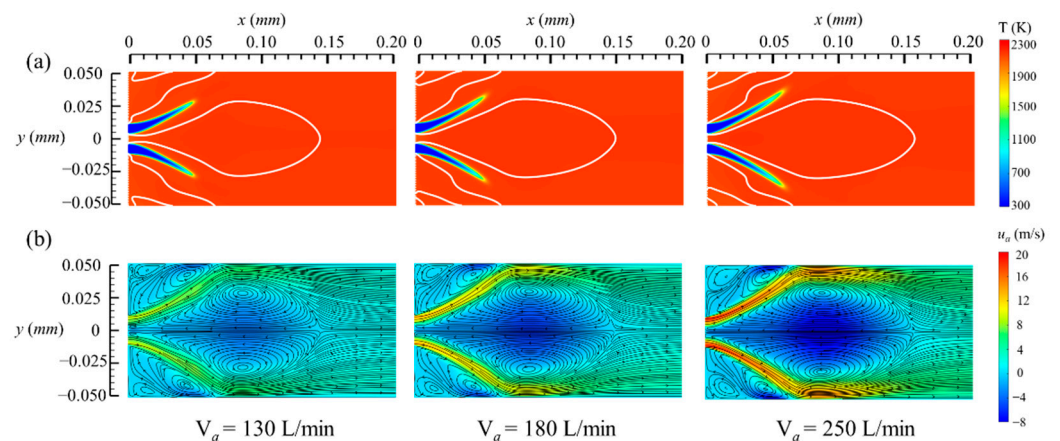


Figure 7. (a) Temperature contour along with zero axial velocity isolines, and (b) axial velocity contour along with the streamlines of different V_a , where $S_N = 0.45$ and $T_i = 300$ K.

The effect of inlet air flow rate on pressure oscillations is shown in Figure 8. As V_a is increased, the pressure fluctuation amplitude was dramatically raised and reached approximately 1500 Pa at $V_a = 250$ L/min. It is worth noting that the amplitude of pressure at $V_a = 250$ L/min is not stable, and there is an obvious fluctuation of the envelope of pressure signal, which indicates intensive thermoacoustic oscillation. It can be seen from Figure 9 that the dominant frequency of pressure oscillation is increased with the increase of V_a , from 294 Hz at $V_a = 130$ L/min to 306 Hz at $V_a = 250$ L/min.

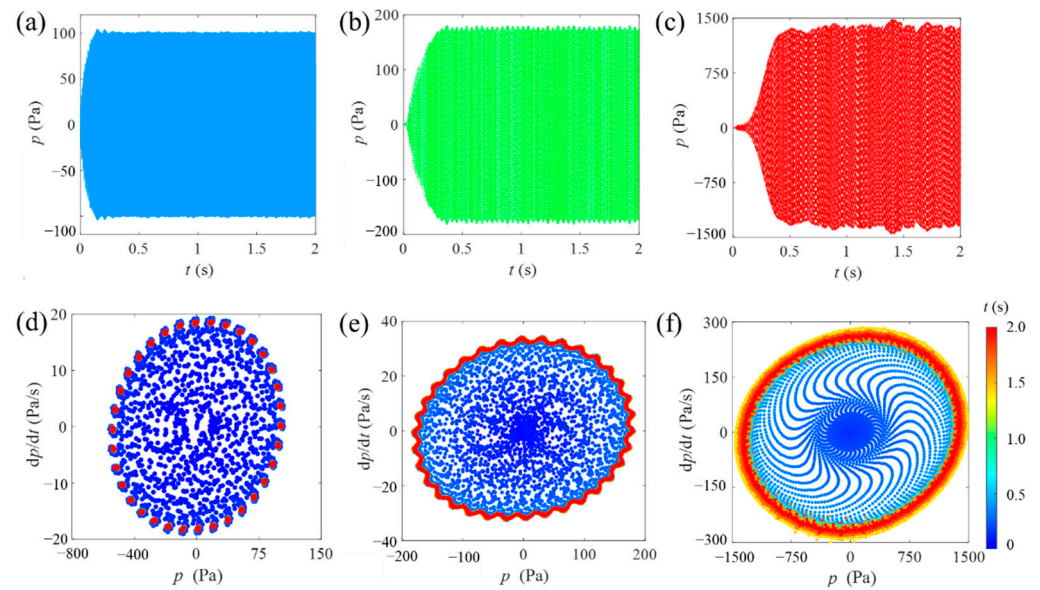


Figure 8. (a–c) Time domain signal of pressure fluctuations and (d–f) corresponding phase diagram. (a) and (d) $V_a = 130$ L/min, (b) and (e) $V_a = 180$ L/min, and (c) and (f) $V_a = 250$ L/min, where $S_N = 0.45$ $T_i = 300$ K.

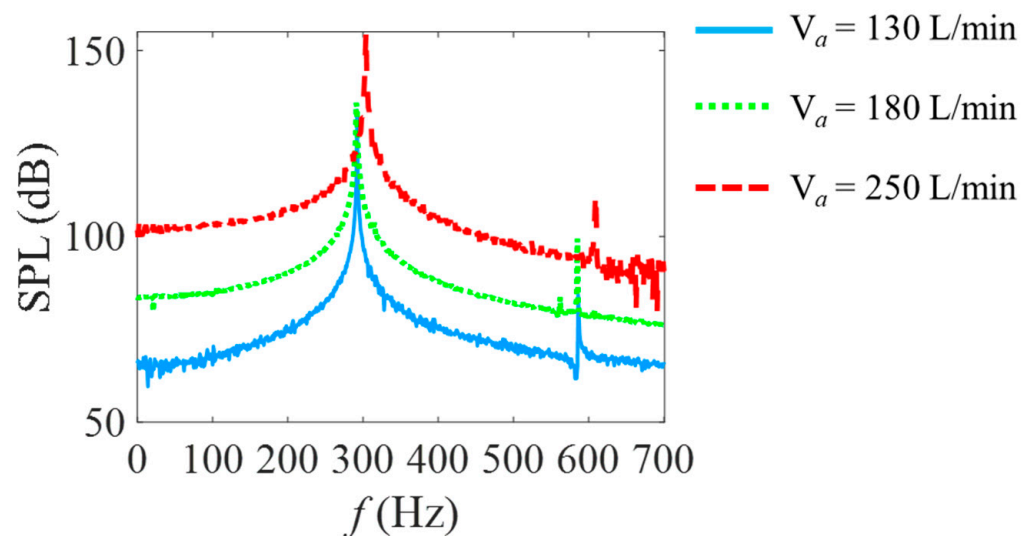


Figure 9. Frequency spectrum of acoustic pressure fluctuation of different V_a at $S_N = 0.45$ and $T_i = 300$ K.

3.4. Effect of Incoming Preheated Air Temperature T_i

Incoming air temperature could also affect the resulting combustion instability. Its effect is examined in Figure 10, which shows the axial velocity and temperature distributions at $t = 0$ s with an inlet temperature of 300, 400 and 600 K, respectively. As inlet temperature is increased, CTRZ and CRZ move upstream. The flame length decreases dramatically due to the large burning velocity under high inlet temperature. Figure 10b shows that at a higher inlet temperature, the axial velocity jet layer and reversal axial velocity at CTRZ are smaller. This can be explained by the fact that high inlet temperature weakens the gas thermal expansion effect.

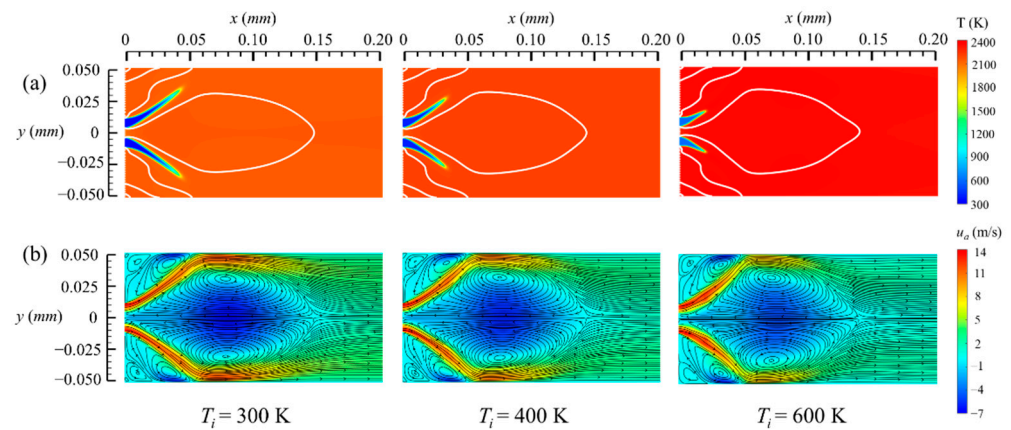


Figure 10. (a) Temperature contour along with zero axial velocity isolines, and (b) axial velocity contour along with streamlines of different T_i , where $S_N = 0.60$ and $V_a = 180$ L/min.

Figure 11a–c shows the time evolution of pressure fluctuations in the swirling combustor, as the inlet temperature is set to 3 different values. It can be observed that with incoming air, the temperature increased from $T_i = 300$ to 400 K, and the amplitude of the generated limit cycles decreased dramatically from 710 Pa to 176 Pa (refer to Figure 11a,b). Further increasing T_i to 600 K led to the amplitude decreasing slightly (refer to Figure 11b,c). Figure 11d–f illustrates the corresponding phase diagrams at different T_i . The ‘annulus-shape’ phase diagrams indicate the presence of multiple tones and thus the nonlinearity of the combustion system.

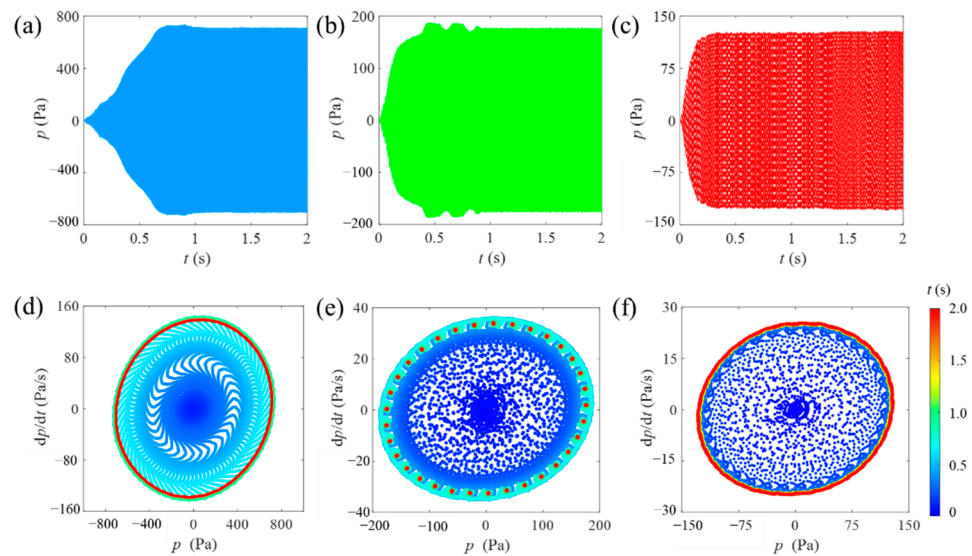


Figure 11. (a–c) Time domain signal of pressure fluctuations and (d–f) corresponding phase diagram. (a,d) $T_i = 300$ K, (b,e) $T_i = 400$ K, and (c,f) $T_i = 600$ K, where $S_N = 0.6$ and $V_a = 180$ L/min.

Further assessment is carried out by determining the pressure spectrum, as shown in Figure 12. It can be seen that there are fundamental peaks at approximately 300 Hz and its harmonics. In addition, as the incoming air temperature is varied, the dominant mode frequency is found to shift slightly at around 300 Hz. Finally, increasing T_i from 300 K to 600 K leads to a reduction of about 17 dB. This reveals that mitigating self-excited thermoacoustic instability in this modelled swirling combustor could be achieved by increasing the incoming air temperature using methods such as pre-heating technology. The damping effect could be mainly due to the reduction of the temperature gradient between pre- and after-combustion regions. Further studies are needed in future work to optimize the incoming air temperature and minimize thermoacoustic instability.

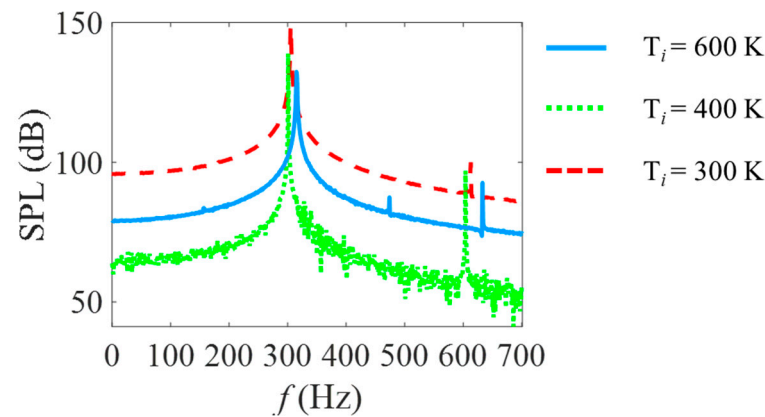


Figure 12. Frequency spectrum of acoustic pressure fluctuations of different T_i at $S_N = 0.6$ and $V_a = 180$ L/min.

4. Further Investigations into the Heat Exchanger Temperature T_H Effect

Energy transfer from heat to sound is undesirable in gas turbine combustors. However, acoustic energy is used to do work in thermoacoustic devices such as thermoacoustic engines. Thus, it is significant to understand the amplification and suppression mechanism of thermoacoustic oscillations. In this section, the effect of a heat exchanger, positioned on the combustor wall, on the excitation and mitigation of thermoacoustic oscillation is investigated. This part of the present work aims to discuss and demonstrate the possibility of using this method in the swirling combustor, and only qualitative research is conducted. In the present study, an iso-thermal wall boundary condition at different temperatures is applied to imitate the heat-loss effect of the practical combustor. At first, the heat exchanger temperature, T_H , is set to $T_H = 500$ K, which is a large heat-loss operation condition. The heat exchanger temperature is increased to $T_H = 1800$ K at $t \geq 2$ s, which is a low heat-loss operation condition. In practical applications, due to heat loss already existing in the combustor wall, this effect can be achieved by reducing the coolant flow or by wrapping it with thermal insulation materials. Pressure fluctuations data are collected from the probe at $x = 328$ mm on the axial center line. Figure 13a shows the time domain signal of pressure fluctuations in the combustor, where $S_N = 0.45$, $V_a = 180$ L/min and $T_i = 300$ K. It is worth noting that pressure oscillation amplitude is amplified and reaches around 1550 a, compared with the model with no heat exchanger in Figure 8b. When the heat exchanger temperature is increased to $T_H = 1800$ K, the pressure oscillation amplitude decreases gradually and becomes stable at the small amplitude of the 215 Pa limit cycle. Here, acoustic energy is introduced to evaluate the heat-to-sound conversion. Acoustic energy per unit volume in time domain $E_a(t)$ is given as [39]:

$$E_a(t) = \frac{1}{\tau} \frac{\int_{\tau} (p')^2 dt}{2\gamma p_0} \quad (6)$$

where $\gamma = 1.4$ is the gas adiabatic constant. p' is the pressure fluctuation in the time domain. p_0 is the reference atmosphere pressure, and τ is the pressure oscillation period. Figure 13b illustrates that over 90% of acoustic energy is reduced by increasing T_H . Figure 13c compares the spectrum of pressure fluctuations before and after T_H is increased. It can be seen that the dominant frequency shifts from 291 Hz to 295 Hz. As for the $T_H = 1800$ K case, a local peak at the harmonic frequency of 590 Hz is observed clearly.

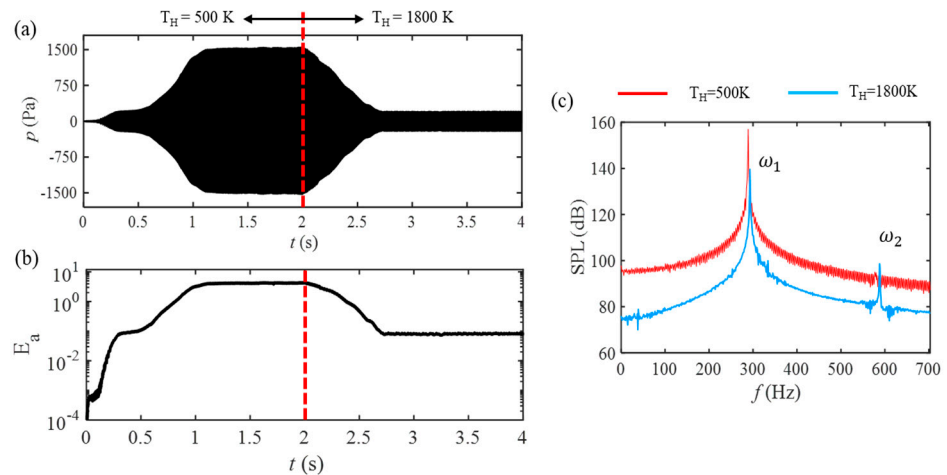


Figure 13. (a) Pressure fluctuation in the time domain, (b) acoustic energy per unit volume in the time domain, and (c) corresponding spectrum of pressure fluctuations, where $S_N = 0.45$, $V_a = 180$ L/min and $T_i = 300$ K.

To reveal how the heat changer affects the flow field characteristics in the combustor, Figures 14 and 15 illustrate the temperature contours with streamlines and isolines of zero value for the axial velocity over an oscillation period before and after T_H is increased. Flow fields are changed dramatically at $T_H = 500$ K, as Figure 15a–d shows. In the first half of the cycle, negative pressure fluctuation in the combustor reaches its minimum value at $\tau/4$ and returns to 0 at $\tau/2$. The area of the recirculating zone is maximum at $\tau/2$. In the other half of the cycle, pressure in the fluctuation combustor has a positive value. CRZ and CTRZ are compressed. The areas recede and reach their minimum at τ . In this process, back flow gas is cooled first due to the heat exchanger and then heated by flame, which increases the pressure amplitude and reinforces the vibration. This is the reason why combustion can sustain such large amplitude oscillation at $T_H = 500$ K. After T_H is increased to 1800 K, it can be seen from Figure 15a,b that the area and shape of the recirculation zone are almost unchanged over a period. The uniformity of the temperature field inside the combustor is improved, which reduces the amplifying effect mentioned before and suppress thermoacoustic oscillation.

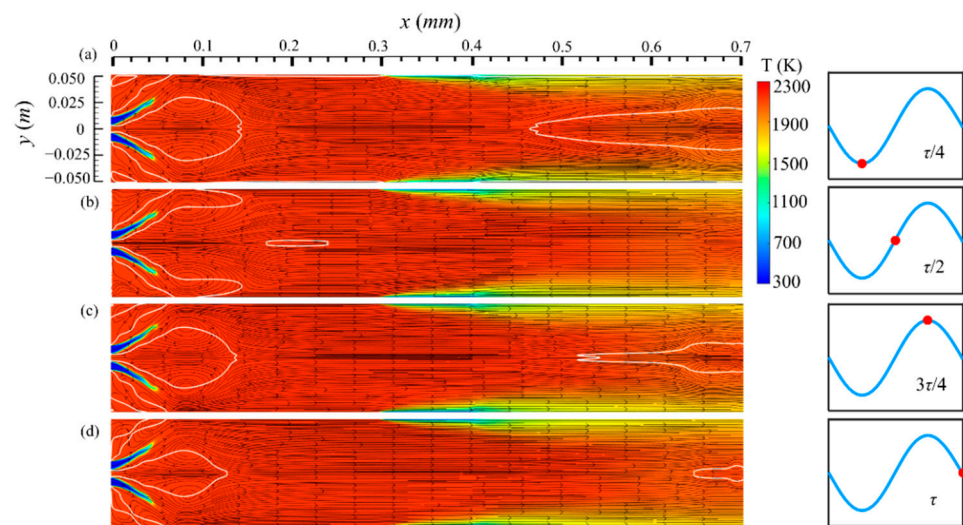


Figure 14. Temperature contour along with zero axial velocity isolines and streamlines and over a period. (a) $\tau/4$ (b) $\tau/2$ (c) $3\tau/4$ and (d) τ at $T_H = 500$ K, where $S_N = 0.45$, $V_a = 180$ L/min and $T_i = 300$ K.

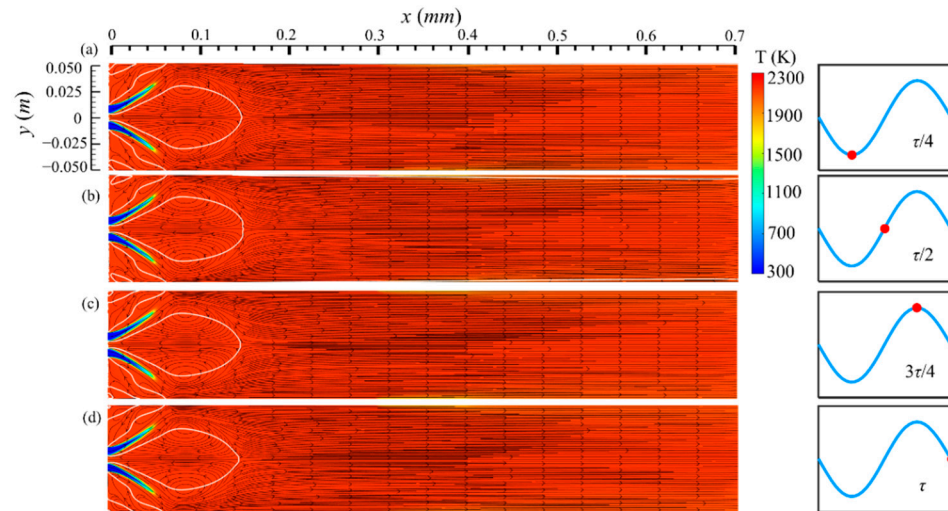


Figure 15. Temperature contour along with zero axial velocity isolines and streamlines and over a period. (a) $\tau/4$ (b) $\tau/2$ (c) $3\tau/4$ and (d) τ at $T_H = 1800$ K, where $S_N = 0.45$, $V_a = 180$ L/min and $T_i = 300$ K.

Figure 16a compares the radical variation of instantaneous over an oscillation period at the $x/R_c = 1.2$ cross section, before and after T_H is increased. The axial velocity oscillation ranges at $T_H = 500$ K are much wider than at $T_H = 1800$ K. The axial velocity fluctuations at the maximum axial velocity point are used to carry out frequency spectrum analysis, as shown in Figure 16b. Increasing T_H reduces the amplitude of axial velocity fluctuation by over 90%. The dominant frequency is found to shift from 291 Hz to 295 Hz.

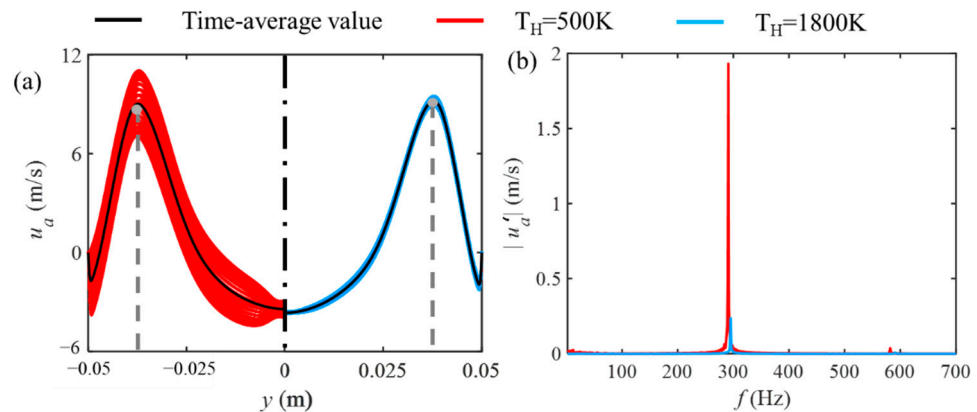


Figure 16. (a) Radical variation of instantaneous over an oscillation period at the $x/R_c = 1.2$ cross section for $T_H = 500$ K (left) and $T_H = 1800$ K (right). (b) Corresponding axial velocity frequency spectrum at the maximum axial velocity value point, where $S_N = 0.45$, $V_a = 180$ L/min and $T_i = 300$ K.

To shed lights on the generation and damping of thermoacoustic instability, Rayleigh index analysis is then conducted to further characterize self-sustained thermo-acoustic coupling [40]. The Rayleigh index is widely applied to indicate the unsteady coupling nature between pressure and heat release perturbation [41]. The local Rayleigh index distribution can be calculated as [42]:

$$RI = \frac{1}{\tau} \int \frac{p'(x, y, z, t)q'(x, y, z, t)}{p_{rms}\bar{q}} dt \tag{7}$$

where p' and q' are the acoustic pressure and unsteady heat release oscillation, which are all the function of spatial locations and time. p_{rms} is the root mean square value of

pressure, and \bar{q} is the time average heat release rate. Figure 17 shows the local contour map of the Rayleigh index at $T_H = 500$ K and $T_H = 1800$ K. As shown in the contours, the positive zone with red color denotes the driving effect (constructive interaction between thermo-acoustic couplings) on limit cycle oscillations, i.e., thermoacoustic instabilities. However, the negative value region with a blue color has a damping effect (destructive interaction) on limit cycle oscillations. As can be seen from Figure 18a, there is a stratified structure pattern of local Rayleigh index distribution. Positive value regions and negative ones are periodically presented in space. Closer observation reveals that the maximum driving/generation effect in the region occurs at 0.05 m in the axial direction and ± 0.03 m along the radial direction, which corresponds to the shear layer and flame tips. Referring to the streamlines in Figures 14 and 17b illustrates the local Rayleigh index distribution, as the heat exchanger temperature is set to $T_H = 1800$ K. This is quite different from the contour at $T_H = 500$ K, as shown in Figure 17a. The patterns of positive and negative value zones are not periodically presented any more. The positive and negative value regions with smaller values of the local Rayleigh index intertwine with each other.

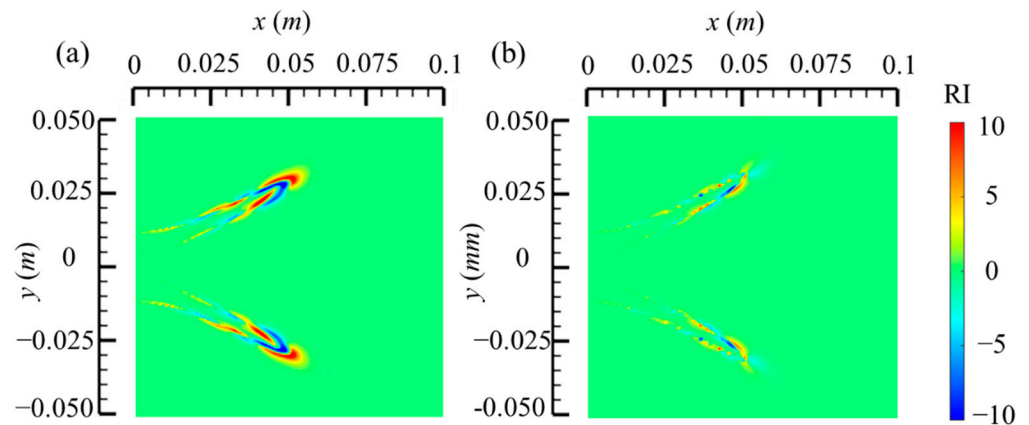


Figure 17. Local Rayleigh Index distribution: (a) $T_H = 500$ K and (b) $T_H = 1800$ K, where $S_N = 0.45$, $V_a = 180$ L/min and $T_i = 300$ K.

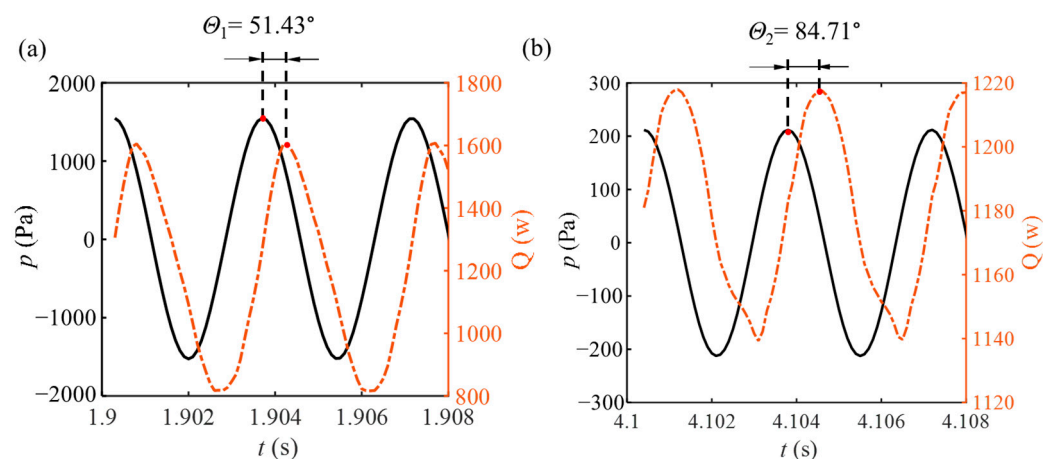


Figure 18. Global Rayleigh Index analysis: phase difference between the pressure and heat release fluctuations (a) $T_H = 500$ K and (b) $T_H = 1800$ K, where $S_N = 0.45$, $V_a = 180$ L/min and $T_i = 300$ K.

Moreover, global coupling between pressure and global heat release rate fluctuation can be characterized by their phase difference of perturbations [43], as shown in Figure 18. According to Rayleigh criterion [44], if the fluctuations of pressure and heat release are in the same phase, such as between -90° to 90° , there is a driving effect. If the phase difference is close to 90° or -90° , the driving effect is minimum. As illustrated in Figure 18,

phase difference between pressure and heat release fluctuations at 1800 K is larger than at 500 K, and it is close to 90° , which also indicates that thermoacoustic instability is suppressed successfully.

5. Conclusions

In the present work, 3D URANS simulations are conducted to study the nonlinear self-sustained thermoacoustic oscillations in a modelled swirling combustor. Turbulence and combustion models are the RNG $k-\varepsilon$ model and EDC model, respectively. A global 2-step combustion kinetic mechanism is applied to deal with chemical reactions. The effect of swirling number S_N , inlet air flow rate V_a and inlet temperature T_i on mean temperature and flow fields, as well as the swirling combustion-excited limit cycle oscillation characteristics, are examined. Recirculation zone structures are highly affected by S_N . As S_N is increased, the wake recirculation zone (WRZ) disappears, and the central toroidal recirculation zone (CTRZ) and corner recirculation zone (CRZ) move upstream. As S_N is increased, the amplitude and dominant frequency of acoustic pressure oscillations is also increased. As inlet air flow rate V_a is increased as the recirculation zone moves downstream. Increasing V_a results in the increase of both the amplitude and frequency of acoustic pressure fluctuations. The increase of inlet air temperature, T_i , causes the reduction of flame length and the CTRZ shrink to upstream. Increasing T_i from 300 K to 600 K results in about a 17 dB reduction of sound pressure level (SPL).

Further investigation into the amplification and mitigation effect on combustion-driven limit cycle oscillations is studied by installing an adjustable temperature heat exchanger on the combustion chamber wall. Thermoacoustic oscillations in the swirling combustor can be successfully amplified or suppressed by a lower or higher heat exchanger temperature, T_H . The acoustic amplitude, acoustical energy and axial velocity fluctuation range are dramatically reduced with the increase of T_H . The dominant frequency of the acoustic pressure and axial velocity spectrum are found to be involved in a 1.6% shift to a higher frequency. A non-negligible harmonic frequency peak is observed in the acoustic pressure spectrum in the high T_H condition. Finally, both local and global Rayleigh index analyses are conducted to investigate unsteady and dynamic coupling between acoustic perturbations and unsteady heat release. Increasing T_H is found to weaken the strong driving/generating effect in shear layers and the flame tips region to prevent and/or mitigate combustion instability. The present study is conducive to developing a simulation platform for thermoacoustic instabilities in swirling combustors. This paper also proposes an alternative method by using a heat exchanger and sheds light on its excitation and mitigation effects to strengthen or weaken thermoacoustic oscillations in swirling combustion systems.

Author Contributions: Y.S. conducted numerical simulations. Y.S. processed and analysed the data and discussed the results with D.Z. and X.Z., D.Z. conceived and initialized the project. All authors contributed to the paper writing and English editing. All authors have read and agreed to the published version of the manuscript.

Funding: This research was funded by the University of Canterbury, New Zealand with Grant No. 452STUPDZ, and National Research Foundation, Prime Minister's Office, Singapore, with Grant No. NRF2016NRF-NSFC001-102 and National Natural Science Foundation of China (No.11661141020).

Institutional Review Board Statement: Not applicable.

Informed Consent Statement: Not applicable.

Data Availability Statement: Not applicable.

Conflicts of Interest: The authors declare no conflict of interest.

Nomenclature

S_N	Swirling number
V_a	Inlet air flow rate
T_i	Inlet temperature
T_H	Heat exchanger temperature
ρ	Density
p	pressure
t	time
\vec{v}	velocity vector
τ'_{ij}	Reynolds stress tensor
E	total energy
k_{eff}	effective thermal conductivity
h_i	enthalpy of species i
\vec{J}_i	diffusion flux of species i
S_h	Fluid enthalpy source
Y_i	Mass fraction of species i
ω_i	Net rate of species i
R_g	Universal gas constant
M_w	mean molecular weight
E_a	Acoustic energy
γ	Gas adiabatic index
p'	Pressure fluctuation
p_0	reference pressure
τ	Oscillation period
γ	Gas adiabatic index
γ	Gas adiabatic index
γ	Gas adiabatic index
RI	Local Rayleigh index
q'	Heat release fluctuation
p_{rms}	Root mean square value of pressure
\bar{q}	Time average heat release rate
Θ	Phase difference

Abbreviations

RANS	Reynolds-averaged Navier-Stokes
URANS	Unsteady Reynolds-averaged Navier-Stokes
RNG	Re-Normalization Group
EDC	Eddy-dissipation-concept
WRZ	Wake recirculation zone
CRZ	corner recirculation zone
CTRZ	central toroidal recirculation zone
SPL	sound pressure level

Appendix A

The simulated results with a whole calculation domain and a 1/8 sector are compared in this part. Figure A1 depicts the radical mean axial velocity profiles for two simulation domains at different cross sections. Figure A2 presents a comparison of the frequency spectrum of pressure fluctuation monitored at the probe. It can be seen that the mean axial velocity profiles are almost identical when using the full scale and the 1/8 sector. For the frequency spectrum, there is a minor difference in pressure fluctuation amplitude and frequency. Since the difference between the two computational domains is slight, the compromise between simulation accuracy and cost is made.

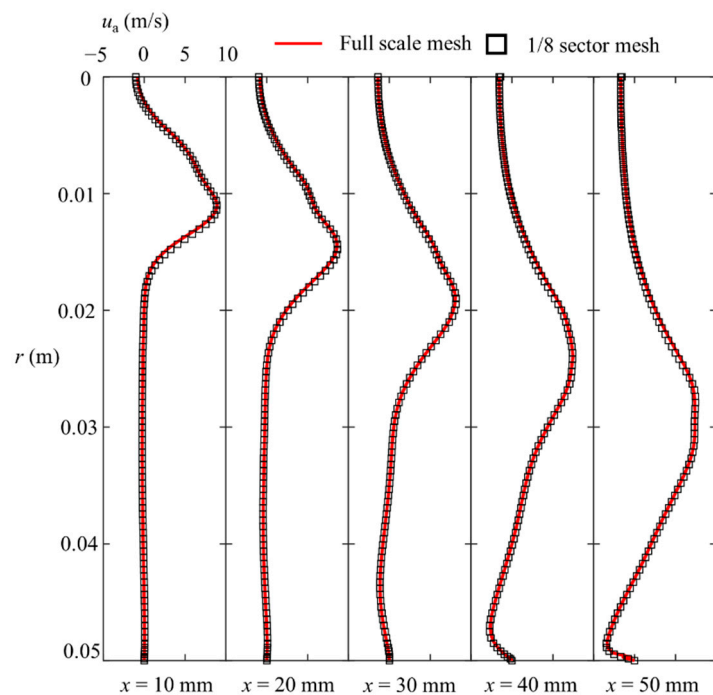


Figure A1. Radical profiles of axial velocity comparison.

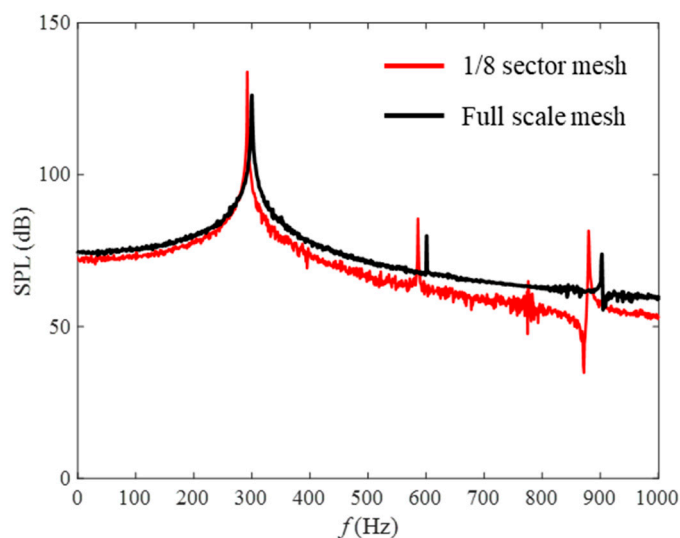


Figure A2. Frequency spectrum comparison.

References

1. Yang, D.; Laera, D.; Morgans, A.S. A systematic study of nonlinear coupling of thermoacoustic modes in annular combustors. *J. Sound Vib.* **2019**, *456*, 137–161. [\[CrossRef\]](#)
2. Jiang, D.; Yang, W.; Teng, J. Entropy generation analysis of fuel lean premixed CO/H₂/air flames. *Int. J. Hydrog. Energy* **2015**, *40*, 5210–5220. [\[CrossRef\]](#)
3. Candel, S. Combustion dynamics and control: Progress and challenges. *Proc. Combust. Inst.* **2002**, *29*, 1–28. [\[CrossRef\]](#)
4. Wang, W.; Liu, J.; Zuo, Z.; Yang, W. Entropy generation analysis of unsteady premixed methane/air flames in a narrow channel. *Appl. Therm. Eng.* **2017**, *126*, 929–938. [\[CrossRef\]](#)
5. Li, L.; Yang, L.; Sun, X. Effect of distributed heat source on low frequency thermoacoustic instabilities. *J. Sound Vib.* **2013**, *332*, 3098–3111. [\[CrossRef\]](#)
6. Keller, J.J. Thermoacoustic oscillations in combustion chambers of gas turbines. *Aiaa J.* **1995**, *33*, 2280–2287. [\[CrossRef\]](#)
7. Lieuwen, T. Modeling premixed combustion-acoustic wave interactions: A review. *J. Propul. Power* **2003**, *19*, 765–781. [\[CrossRef\]](#)

8. Correa, S.M. Carbon monoxide emissions in lean premixed combustion. *J. Propul. Power* **1992**, *8*, 1144–1151. [[CrossRef](#)]
9. Yi, T.X.; Santavicca, D.A. Combustion Instability and Flame Structure of Turbulent Swirl-Stabilized Liquid-Fueled Combustion. *J. Propul. Power* **2012**, *28*, 1000–1014. [[CrossRef](#)]
10. Mariappan, S.; Sujith, R.I. Thermoacoustic instability in a solid rocket motor: Non-normality and nonlinear instabilities. *J. Fluid. Mech.* **2010**, *653*, 1–33. [[CrossRef](#)]
11. Lucca-Negro, O.; O'Doherty, T. Vortex breakdown: A review. *Prog. Energy Combust.* **2001**, *27*, 431–481. [[CrossRef](#)]
12. Galley, D.; Ducruix, S.; Lacas, F.; Veynante, D. Mixing and stabilization study of a partially premixed swirling flame using laser induced fluorescence. *Combust. Flame* **2011**, *158*, 155–171. [[CrossRef](#)]
13. Candel, S.; Durox, D.; Schuller, T.; Bourgooin, J.-F.; Moeck, J.P. Dynamics of swirling flames. *Annu. Rev. Fluid Mech.* **2014**, *46*, 147–173. [[CrossRef](#)]
14. Syred, N.; Beer, J. Combustion in swirling flows: A review. *Combust. Flame* **1974**, *23*, 143–201. [[CrossRef](#)]
15. Kim, J.; Jang, M.; Lee, K.; Masri, A.R. Experimental study of the beating behavior of thermoacoustic self-excited instabilities in dual swirl combustors. *Exp. Therm. Fluid Sci.* **2019**, *105*, 1–10. [[CrossRef](#)]
16. Han, X.; Laera, D.; Morgans, A.S.; Lin, Y.; Sung, C.-J. The effect of stratification ratio on the macrostructure of stratified swirl flames: Experimental and numerical Study. *J. Eng. Gas. Turbines Power* **2018**, *140*, 121004. [[CrossRef](#)]
17. Karlis, E.; Liu, Y.S.; Hardalupas, Y.; Taylor, A.M.K.P. H-2 enrichment of CH₄ blends in lean premixed gas turbine combustion: An experimental study on effects on flame shape and thermoacoustic oscillation dynamics. *Fuel* **2019**, *254*. [[CrossRef](#)]
18. Bonciolini, G.; Ebi, D.; Doll, U.; Weilenmann, M.; Noiray, N. Effect of wall thermal inertia upon transient thermoacoustic dynamics of a swirl-stabilized flame. *Proc. Combust. Inst.* **2019**, *37*, 5351–5358. [[CrossRef](#)]
19. Pausch, K.; Herff, S.; Schröder, W. Noise sources of an unconfined and a confined swirl burner. *J. Sound Vib.* **2020**, *475*, 115293. [[CrossRef](#)]
20. Huang, Y.; Yang, V. Effect of swirl on combustion dynamics in a lean-premixed swirl-stabilized combustor. *Proc. Combust. Inst.* **2005**, *30*, 1775–1782. [[CrossRef](#)]
21. Choi, J.; Rusak, Z.; Kapila, A. Numerical simulation of premixed chemical reactions with swirl. *Combust. Theor. Model.* **2007**, *11*, 863–887. [[CrossRef](#)]
22. Choi, M.; Park, Y.; Li, X.; Sung, Y.; Park, S.; Moon, K.; Choi, G. Study on flame structures and emission characteristics according to various swirl combinations and fuel compositions in a CH₄/H₂/CO syngas swirl-stabilized combustor. *Fuel* **2019**, *253*, 887–903. [[CrossRef](#)]
23. Noiray, N.; Schuermans, B. Theoretical and experimental investigations on damper performance for suppression of thermoacoustic oscillations. *J. Sound Vib.* **2012**, *331*, 2753–2763. [[CrossRef](#)]
24. Zhang, G.; Wang, X.; Li, L.; Jing, X.; Sun, X. Control of thermoacoustic instability with a drum-like silencer. *J. Sound Vib.* **2017**, *406*, 253–276. [[CrossRef](#)]
25. DeLaat, J.C.; Kopasakis, G.; Saus, J.R.; Chang, C.T.; Wey, C. Active combustion control for a low-emissions aircraft engine combustor prototype: Experimental results. *J. Propul. Power* **2013**, *29*, 991–1000. [[CrossRef](#)]
26. Paschereit, C.O.; Gutmark, E.; Weisenstein, W. Control of thermoacoustic instabilities and emissions in an industrial-type gas-turbine combustor. *Symp. (Int.) Combust.* **1998**, *27*, 1817–1824. [[CrossRef](#)]
27. Hong, Z.; Dai, X.; Zhou, N.; Sun, X.; Jing, X. Suppression of Helmholtz resonance using inside acoustic liner. *J. Sound Vib.* **2014**, *333*, 3585–3597. [[CrossRef](#)]
28. Gelbert, G.; Moeck, J.P.; Paschereit, C.O.; King, R. Feedback control of unstable thermoacoustic modes in an annular Rijke tube. *Control. Eng. Pract.* **2012**, *20*, 770–782. [[CrossRef](#)]
29. Lei, L.; Zhihui, G.; Chengyu, Z.; Xiaofeng, S. A Passive Method to Control Combustion Instabilities with Perforated Liner. *Chin. J. Aeronaut.* **2010**, *23*, 623–630. [[CrossRef](#)]
30. Williams, L.J.; Meadows, J.; Agrawal, A.K. Passive control of thermoacoustic instabilities in swirl-stabilized combustion at elevated pressures. *Int. J. Spray Combust. Dyn.* **2016**, *8*, 173–182. [[CrossRef](#)]
31. Li, S.; Li, Q.; Tang, L.; Yang, B.; Fu, J.; Clarke, C.A.; Jin, X.; Ji, C.Z.; Zhao, H. Theoretical and experimental demonstration of minimizing self-excited thermoacoustic oscillations by applying anti-sound technique. *Appl. Energy* **2016**, *181*, 399–407. [[CrossRef](#)]
32. Wu, G.; Lu, Z.; Pan, W.; Guan, Y.; Li, S.; Ji, C.Z. Experimental demonstration of mitigating self-excited combustion oscillations using an electrical heater. *Appl. Energy* **2019**, *239*, 331–342. [[CrossRef](#)]
33. Wu, G.; Xu, X.; Li, S.; Ji, C. Experimental studies of mitigating premixed flame-excited thermoacoustic oscillations in T-shaped Combustor using an electrical heater. *Energy* **2019**, *174*, 1276–1282. [[CrossRef](#)]
34. Mahesh, S.; Gopakumar, R.; Rahul, B.; Dutta, A.; Mondal, S.; Chaudhuri, S. Instability control by actuating the swirler in a lean premixed combustor. *J. Propul. Power* **2018**, *34*, 708–719. [[CrossRef](#)]
35. Sun, Y.; Rao, Z.; Zhao, D.; Wang, B.; Sun, D.; Sun, X. Characterizing nonlinear dynamic features of self-sustained thermoacoustic oscillations in a premixed swirling combustor. *Appl. Energy* **2020**, *264*, 114698. [[CrossRef](#)]
36. Chen, S.; Zhao, D. Numerical study of guide vane effects on reacting flow characteristics in a trapped vortex combustor. *Combust. Sci. Technol.* **2018**, *190*, 2111–2133. [[CrossRef](#)]
37. Westbrook, C.K.; Dryer, F.L. Simplified reaction mechanisms for the oxidation of hydrocarbon fuels in flames. *Combust. Sci. Technol.* **1981**, *27*, 31–43. [[CrossRef](#)]

38. Zhang, M.; Wei, X.; Wang, J.; Huang, Z.; Tan, H. The blow-off and transient characteristics of co-firing ammonia/methane fuels in a swirl combustor. *Proc. Combust. Inst.* **2020**. [[CrossRef](#)]
39. Zhao, D.; Guan, Y.; Reinecke, A. Characterizing hydrogen-fuelled pulsating combustion on thermodynamic properties of a combustor. *Commun. Phys.* **2019**, *2*. [[CrossRef](#)]
40. Yilmaz, İ.; Ratner, A.; Ilbas, M.; Huang, Y. Experimental investigation of thermoacoustic coupling using blended hydrogen–methane fuels in a low swirl burner. *Int. J. Hydrog. Energy* **2010**, *35*, 329–336. [[CrossRef](#)]
41. Song, H.; Lin, Y.; Han, X.; Yang, D.; Zhang, C.; Sung, C.-J. The thermoacoustic instability in a stratified swirl burner and its passive control by using a slope confinement. *Energy* **2020**, *195*, 116956. [[CrossRef](#)]
42. Huang, Y.; Ratner, A. Experimental investigation of thermoacoustic coupling for low-swirl lean premixed flames. *J. Propul. Power* **2009**, *25*, 365–373. [[CrossRef](#)]
43. Bragg, S.L. Noise and Oscillations in Jet Engines. *Nature* **1964**, *201*, 123. [[CrossRef](#)]
44. Rayleigh, L. The explanation of certain acoustical phenomena. *Nature* **1878**, *18*, 319–321. [[CrossRef](#)]